

Theoretical investigation of two-dimensional phosphorus carbides as promising anode materials for lithium-ion batteries

*Ke Fan^a, Yiran Ying^a, Xin Luo^{*b}, and Haitao Huang^{*a}*

^aDepartment of Applied Physics, The Hong Kong Polytechnic University, Hung Hom,
Kowloon, Hong Kong, P.R. China

^bSchool of Physics, Sun Yat-sen University, Guangzhou, Guangdong Province, P.R.
China, 510275

AUTHOR INFORMATION

Corresponding Author

*E-mail: aphhuang@polyu.edu.hk (H.H.); luox77@mail.sysu.edu.cn (X.L.)

ABSTRACT.

Employing two-dimensional (2D) materials as anodes for lithium-ion batteries (LIBs) is believed to be an effective approach to meet the growing demands of high-capacity next-generation LIBs. In this work, the first-principles density functional theory (DFT) calculations are employed to evaluate the potential application of two-dimensional phosphorus carbide (2D PC_x , $x=2, 5$, and 6) monolayers as anode materials for lithium-ion batteries. The 2D PC_x systems are predicted to show outstanding structural stability and electronic properties. From the nudged elastic band calculations, the Li atoms show extreme high diffusivities on the PC_x monolayer with low energy barriers of 0.18 eV for PC_2 , 0.47 eV for PC_5 , and 0.44 eV for PC_6 . We further demonstrate that the theoretical specific capacity of monolayer PC_5 and PC_6 can reach up to 1251.7 and 1235.9 mAh g⁻¹, respectively, several times that of graphite anode used in commercial LIBs. These results suggest that both PC_5 and PC_6 monolayer are promising anode materials for LIBs. Our work opens a new avenue to explore novel 2D materials in energy applications, where phosphorus carbides could be used as high-performance anode in LIBs.

1. Introduction

In recent years, battery systems have made a big contribution to the rapid development of the electronics market.^{1, 2} Among all types of batteries, lithium-ion batteries (LIBs), as one of the greatest successes of clean energy storage technologies, have attracted widespread attention.³⁻⁶ Conventional anode materials in LIBs have a bulk structure with low capacity and high diffusion barrier which hinder their further applications.⁷ Since the successful isolation of graphene from graphite,⁸⁻¹⁰ two-dimensional (2D) materials, such as hexagonal boron nitride,^{11, 12} phosphorene,¹³⁻¹⁵ transition metal dichalcogenides,¹⁶ and MXenes¹⁷⁻¹⁹ have been widely studied and identified as potential anode materials with enhanced electronic properties for LIBs. Despite these efforts, designing 2D anodes with higher capacity and lower diffusion barrier which can be commercialized is still a challenging job for researchers.

It is well-known that graphene and phosphorene are two important 2D materials that have potential applications in LIBs. Graphene shows excellent conductivity and stability, but six carbon atoms can only adsorb one Li ion to form a LiC_6 intercalation.²⁰ As a comparison, one Li atom can be intercalated with two phosphorus atoms in phosphorene, while the disadvantage of phosphorene is the limited stability in air or humid environment.^{21, 22} Since both elemental carbon and phosphorus are reported to form stable 2D monolayers and have similar structures including three-fold coordinated atoms and a hexagonal network,²³⁻²⁵ it is reasonable to believe that compound phosphorus carbides can

be stable as a monolayer and display properties that might even be superior to both constituents. Until now, several phosphorus carbide monolayers have been theoretically predicted to be stable, among which 2D PC has been fabricated successfully through doping C atoms into phosphorus ones.²⁵⁻³¹ Tan et al. have synthesized metallic black phosphorus carbide (β -PC) which has been verified to be stable at the DFT level,²⁶ and Zhang et al. has proposed to use the γ -PC in the LIBs.²⁸ However, the studies of 2D phosphorus carbide as a promising anode material for LIBs are still scarce due to limited 2D candidates and possible structural instability. Recently, Yu et al. have performed extensive structural search for PC_x ($x=2, 3, 5$, and 6) monolayers, and they found that PC_2 (metal), PC_3 (semiconductor with a band gap of 2.15 eV), PC_5 (metal) and PC_6 (semiconductor with a band gap of 0.84 eV) are thermodynamically stable.³⁰ The predicted PC_x structures except for wide-band-gap semiconductor PC_3 , may have potential applications in anodes for LIBs, but theoretical or experimental evidence is lacking.

Inspired by the great potential of PC in LIBs discussed above, in this work, we systematically investigate the stability, electronic and Li storage properties of PC_2 , PC_5 and PC_6 monolayers by means of density functional theory (DFT) calculations. Our calculations reveal that PC_x ($x=2, 5$, and 6) systems show not only excellent thermal and dynamic stability but also high electron and ionic conductivities. The relatively high capacity of PC_5 (1251.7 mAh g⁻¹) and PC_6 (1235.9 mAh g⁻¹) suggesting that both candidates could be promising anode materials for LIBs.

2. Computational methods

Our calculations were performed in the framework of DFT calculations by the Vienna *ab initio* simulation package (VASP).³² The generalized gradient approximation (GGA) with the Perdew-Burke-Ernzerhof (PBE) flavor³³ was chosen as the exchange-correlation functional. Van der Waals interaction was considered by using the semiempirical DFT-D2³⁴ approach. For the calculation of band structures and density of states (DOS), a more accurate HSE06 hybrid functional³⁵ was applied. The plane-wave cut-off energy of 500 eV was employed. To avoid the interlayer interaction, a vacuum layer of 15 Å was added to the slabs. The Brillouin zone was sampled using a Monkhorst-Pack k-point mesh scheme, and the meshes of Γ -centered $13 \times 13 \times 1$ and $6 \times 6 \times 1$ were used for the unit cell and the $2 \times 2 \times 1$ supercell, respectively. The convergence criteria for energy and force were set to be 10^{-5} eV and $0.01 \text{ eV } \text{\AA}^{-1}$, respectively. Charge differential analysis combined with the Bader charge method³⁶ was used to quantitatively estimate the charge redistribution and transfer. The climbing image nudged elastic band (CI-NEB) method³⁷ was applied to calculate the potential energy diffusion pathway and the minimum diffusion energy barrier of lithium ions on the PC_x monolayer.

Phonon dispersion spectra was calculated by Phonopy code³⁸. *Ab initio* molecular dynamics (AIMD)³⁹ simulations with Nosé-Hoover thermostat and NVT ensemble were performed at 300 K with the time step of 2 fs.

The adsorption energy of Li atoms on the PC_x monolayer can be calculated with the following equation⁴⁰:

$$E_{ad} = (E_{PC_xLi_n} - E_{PC_x} - nE_{Li})/n \quad (1)$$

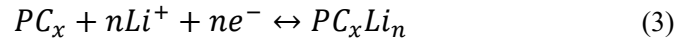
Here, $E_{PC_xLi_n}$ and E_{PC_x} are the total energies of PC_x with and without Li atom adsorption, respectively. E_{Li} represents the energy per Li atom in body-centered cubic (bcc) structure, and n corresponds to the number of Li atoms in the adsorption configurations.

The differential charge density is obtained as the difference between the valence charge density before and after the bonding¹⁹:

$$\Delta\rho = \rho_{PC_xLi_n} - \rho_{Li} - \rho_{PC_x} \quad (2)$$

where $\rho_{PC_xLi_n}$, ρ_{Li} , and ρ_{PC_x} represent the charge density distributions of Li-intercalated PC_x systems, Li atom, and bare PC_x monolayer, respectively.

The charge/discharge processes can be described by the following half-cell reactions:³¹



The open circuit voltage (OCV) at different coverage on the surfaces of the PC_x is calculated as⁴¹⁻⁴³:

$$OCV \approx (E_{PC_x} + nE_{Li} - E_{PC_xLi_n})/n \quad (4)$$

The maximum capacity (C_M) can be obtained by the following equation^{42, 44}:

$$C_M \approx zy_{max}F/M_{PC_x} \quad (5)$$

where z , y_{max} , F , and M_{PC_x} are the valence number, maximum adatom content (corresponding to chemical formula PC_xLi_y), Faraday constant (26.8 Ahmol^{-1})⁴⁵, and relative molecular mass of PC_x , respectively. In the calculation of adsorption process, all

the atoms were fully relaxed.

3. Results and discussion

3.1 Structures and stability

All three DFT-optimized structures of PC_x (shown in Fig. 1 with all optimized lattice constants shown in Table S1) are quasi-planar, with P atoms located away from the basal plane. PC_2 with the space group of P-1 is constructed with 5-8-5 rings, similar to the case of popgraphene.⁴⁶ The 5-ring consists one P atom and four C atoms, while the 8-ring is consisted of four P and four C atoms. Each atom (P and C) is coordinated with two C atoms and one P atom. The other two structures are stabilized into two types of hexagonal structure including C_6 , P_2C_4 rings for PC_5 and C_6 , PC_5 rings for PC_6 (space group P-3). For PC_5 , two types of P_2C_4 rings (ortho-P and para-P) are aligned in a direction and C_6 rings fill up the plane in a zigzag configuration, and each P atom is coordinated with one P atom and two C atoms, similar to the situation of PC_2 . For PC_6 , on the other hand, each C_6 ring is surrounded by six PC_5 rings, and each P is coordinated with three C atoms. The quasi-planar nature of PC_x may provide abundant adsorption sites for practical battery applications.

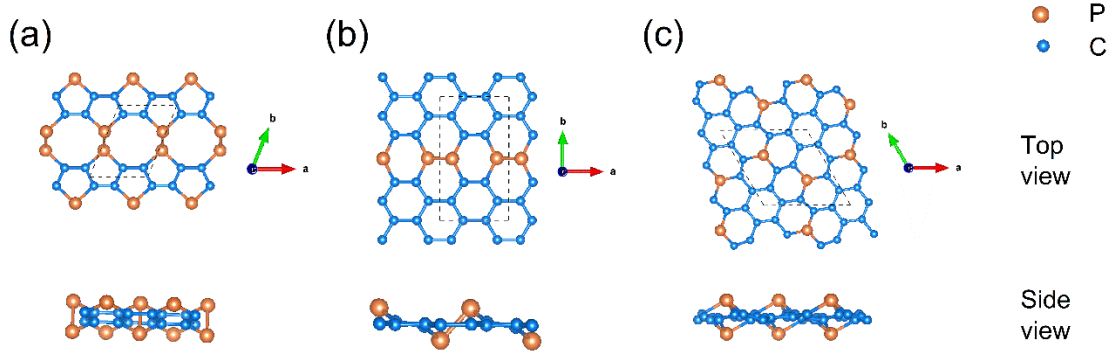


Fig. 1 Top and side views of 2D (a) PC_2 , (b) PC_5 , and (c) PC_6 . The unit cells are indicated by black dashed lines.

The structural stability is a very important factor for practical application of 2D materials. Here, we calculate the phonon dispersion to check the phase stability. Taking PC_5 as an example, in Fig. 2a, the absence of imaginary phonon modes in the first Brillouin zone indicates that PC_5 monolayer is dynamically stable. Furthermore, AIMD simulations are used to examine its thermal stability with 3×3 supercell of PC_5 at 300 K for 10 ps. No obvious structural reconstructions can be noticed as the total energy of the system oscillate around the equilibrium values at the room temperature (Fig. 2b). Similarly, Fig. S1 shows dynamical and thermal stability of PC_2 and PC_6 .

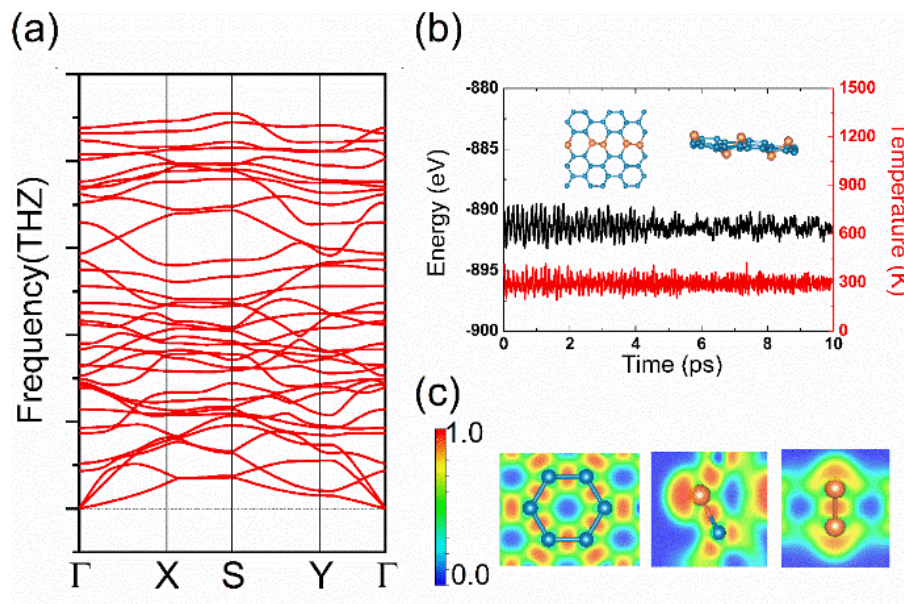


Fig. 2 (a) Phonon dispersion spectra of 2D PC_5 . (b) Total energy and temperature as a function of time for PC_5 during the AIMD simulation (inset: the structure of PC_5 after 10 ps AIMD simulation). (c) Electron localization function (ELF) maps of PC_5 along planes containing specified bonding atoms. P and C atoms are represented in orange and blue, respectively.

The calculated electron localization function (ELF)^{47, 48} clearly describes the bonding behavior. Generally, $ELF > 0.5$ corresponds to a covalent bond or core electrons, whereas the ionic bond is represented by a smaller ELF value (< 0.5). An ELF value of 0.5 is the metallic bond.^{49, 50} For PC_5 , as illustrated in Fig. 2c, the bonds between C-C, P-P and P-C atoms are covalent in nature. Each C atom bonds with the three nearest neighbors in a planar configuration implying that the C atoms are sp^2 hybridized. On the other hand, lone pair electron is shown near P atoms, together with the buckled configuration of PC_5 ,

showing a sp^3 hybridization of P atoms. This bonding configuration satisfying the chemical octet rule on both C and P sites enhances its structure stability. In PC_2 and PC_6 system (Fig. S1), C-C, P-P and C-P bonds also show covalent bond character, with sp^2 hybridization of C atoms and sp^3 hybridization of P atoms. The detailed information about ELF plane is shown in Fig. S2.

3.2 Electronic properties

The electronic structure of anode material strongly correlates with the battery cyclability and rate performance. Since PBE functional usually underestimates the exact band gap values, here, we use more sophisticated hybrid functional HSE06 to perform the electronic structure calculations. Fig. 3 shows the computed density of states (DOS) and electronic band structures. Both PC_2 and PC_5 monolayers show metallic character with one Dirac cone along the Γ -Y direction (Fig. 3a and 3b) which reveal its intrinsic metallicity and high density of carriers, indicating good electronic conductivity. The major contribution to the DOS of the Dirac bands comes from the C atoms with small contribution from the P atoms. The PC_6 monolayer is a direct-gap semiconductor with a band gap of 0.84 eV at the M point (Fig. 3c). Despite its semiconducting nature, PC_6 shows high carrier mobility above $10^5 \text{ cm}^2 \text{ V}^{-1} \text{ s}^{-1}$.³⁰ These features render PC_x as promising candidates for LIBs anodes.

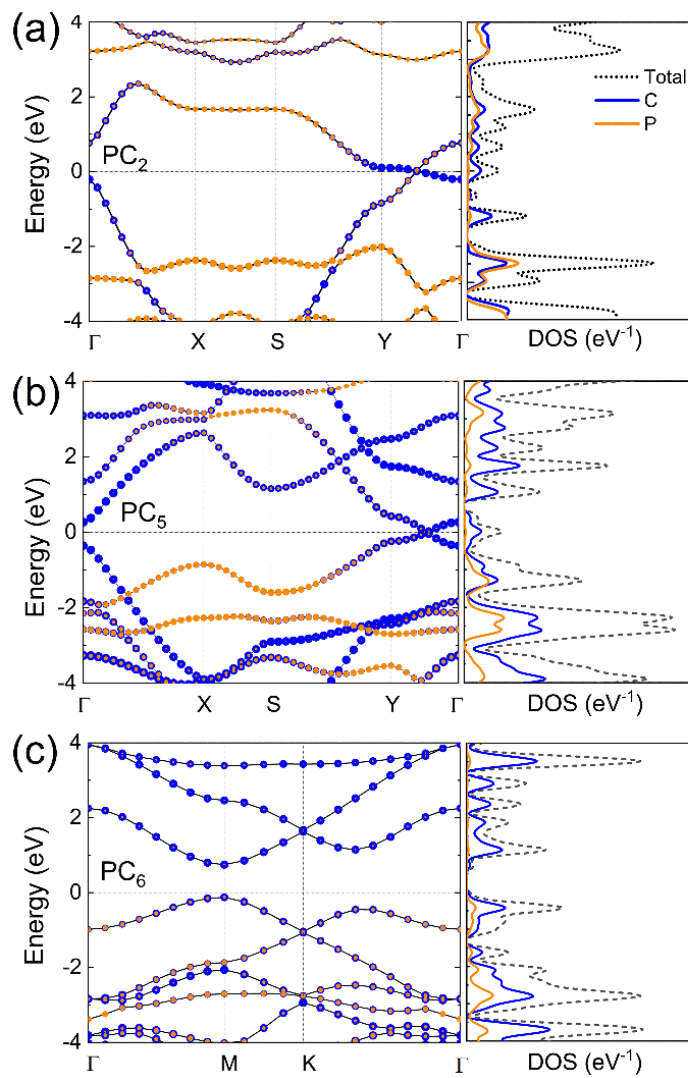


Fig. 3 Electronic band structure (left) and PDOS (right) for 2D (a) PC₂, (b) PC₅ and (c) PC₆ calculated at the HSE06 level. Partial band structure contributed by P and C atoms are represented by orange and blue dots, respectively, and the sizes of the dots are proportional to the weight of the contribution. Fermi levels are set to be zero.

3.3 Investigation of 2D PC_x as anode materials for LIBs

Aside from the stability and electronic structure, the diffusion energy barrier, specific capacity, and open-circuit voltage (OCV) are also the key performance parameters of an anode material for LIBs. To systematically study the adsorption properties, a $2 \times 2 \times 1$ supercell is used to examine the adsorption sites for an isolated Li atom. Several possible high-symmetry adsorption sites are considered (Fig. S3). In PC_2 system, after full structural relaxation, only three inequivalent adsorption sites A1, A2 and A3 are identified. For Li on A1 site, the adsorption energy is -0.94 eV, while for A2 and A3 site, the values are -0.44 eV and -0.87 eV, indicating that A1 is the most favorable adsorption site (Fig. S3a). The adsorption energies are -0.84 and -0.83 eV (Fig. S3b and S3c) for the most favorable A1 sites of PC_5 and PC_6 , respectively. The relatively large adsorption energies of Li atom on PC_x systems ensure the strong adsorption of Li atoms on the anodes.

To visualize the effects of adatom adsorption on the charge distribution, we calculate the differential charge density. Fig. 4 clearly shows the charge transfer from the Li atom to the substrates. Further Bader charge analysis show that each Li transfer 0.89, 0.89, and 0.91 electron to C atoms in PC_2 , PC_5 , and PC_6 , respectively, confirming that the adsorption can be mainly attributed to the interaction between Li and C atom.

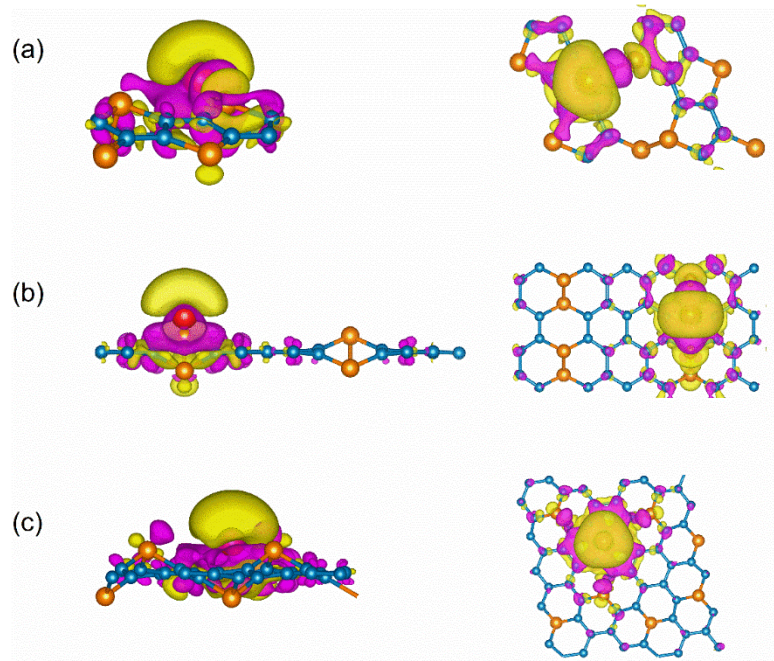


Fig.4 The differential charge density distribution (Left: side view, and Right: top view) of Li adsorption on (a) PC_2 , (b) PC_5 , and (c) PC_6 . Pink and yellow colors indicate electron accumulation and depletion, respectively.

The charge–discharge rate, which depends on the mobility of the intercalating ions, is another significant character for assessing the capability of an electrode material for rechargeable batteries. Therefore, we simulate the motion of Li atom on the surface of PC_x and investigate the diffusion barriers using the CI-NEB method. Based on the adsorption energy of Li atom on several high-symmetry sites (Fig. S3) in each system, color-filled contour plots are presented in Fig. 5 and S4. From the calculated contour plot of total energy (including adsorbed single Li atom) as a function of adsorption site position, the energetically feasible diffusion paths between the nearest-neighboring lowest-energy adsorption sites (A_1 and A_2) are selected. For PC_5 , two possible diffusion pathways are

shown in Fig. 5. For Path 1 ($A_1 \rightarrow B \rightarrow A_2$), the diffusion energy barrier is 0.47 eV with diffusion distance of 7.95 Å. For Path 2 ($A_1 \rightarrow C \rightarrow A_2$), the barrier height is 0.57 eV. For PC_2 and PC_6 , the diffusion energy barrier is 0.18 eV and 0.44 eV with diffusion distances of 4.54 Å and 8.98 Å, respectively (Fig. S4). We note that the diffusion barriers on PC_x are comparable to that on typical 2D materials such as graphene (0.33 eV),^{51, 52} 1T-MoS₂ (0.28 eV),^{53, 54} and MoN₂ (0.78 eV).⁴² The low barriers ensure that Li ions can migrate easily on the surface of our studied systems. Therefore, 2D PC_x systems can be promising electrode materials with fast charge–discharge rate and good rate capability.

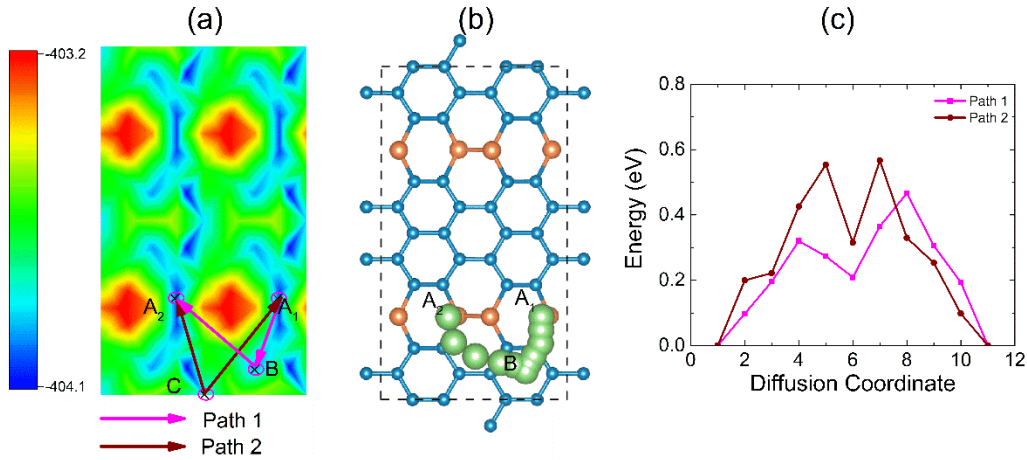


Fig. 5 (a) Schematic illustration of two possible migration paths of Li diffusion on the PC₅ monolayer based on the color-filled contour plots of adsorption energy of Li on the surface of PC₅ monolayer, (b) diffusion of single adatoms over PC₅ monolayer through the favorable pathway (Path 1), and (c) the corresponding diffusion barrier profiles of Li-PC₅.

For practical applications, the storage capacity of batteries is the key indicator for the performance of the electrode materials and the current focus for improvement. To explore the maximum storage capacity for Li atoms, we consider the adsorption with an increasing number of adsorbed Li atoms on both sides of the PC_x monolayers in the 2×2 supercell. To obtain more accurate results, both the atomic positions and lattice constants are fully relaxed for the configurations after the intercalation. The Li atoms are inserted into PC_x systems gradually and randomly until the monolayer reached to its final capacity point. For PC_2 monolayer, two Li atoms can be adsorbed in a single cell at most. Otherwise, the structure will collapse (Fig. S5). Thus, the structural deformation may be caused by the intercalation and deintercalation of Li ions in anodes. Therefore, limiting the deformation which is induced by the Li atoms adsorption is necessary. Here, we conduct a series of AIMD simulations to monitor the structural stability of the Li-intercalated PC_5 and PC_6 nanosheets. Structures with different numbers of adsorbed Li atoms are tested by the simulations to identify the maximum number which does not lead to noticeable deformation of PC_x structures at ambient condition. The AIMD results shown in Fig. 6 present the structures with maximum Li atoms for PC_5 and PC_6 and all the original bonds are kept completely intact. To be specific, the maximum adatom number is 4.25 per PC_5 , i.e. $P_8C_{40}Li_{34}$, over which the structure will collapse (Fig. S6). For, PC_6 , on the other hand, the maximum adatom number is 4.75 (corresponding to chemical formula $P_8C_{48}Li_{38}$), which is judged by the large distance between new adatom and substrate, so that the chemical interactions are too weak to be considered (Fig. S7)^{19, 55}. Thus, the intercalation

of the Li atoms leads to outstanding capacity of 1251.7 and 1235.9 mAh g⁻¹ for PC₅ and PC₆, respectively. The remarkable storage capacities of the phosphorus carbides can be explained by the quasi-planar structures with abundant adsorption sites and relatively small atomic mass of P and C. The calculated OCV as a function of the adatom content y on the PC₅ and PC₆ supercell is plotted in Fig. S8. We can see that the curves for PC₅ and PC₆ show similar trend where the OCV decreases as the number of Li atom y increases at low Li coverage, then converges to a saturated value at higher Li coverage.

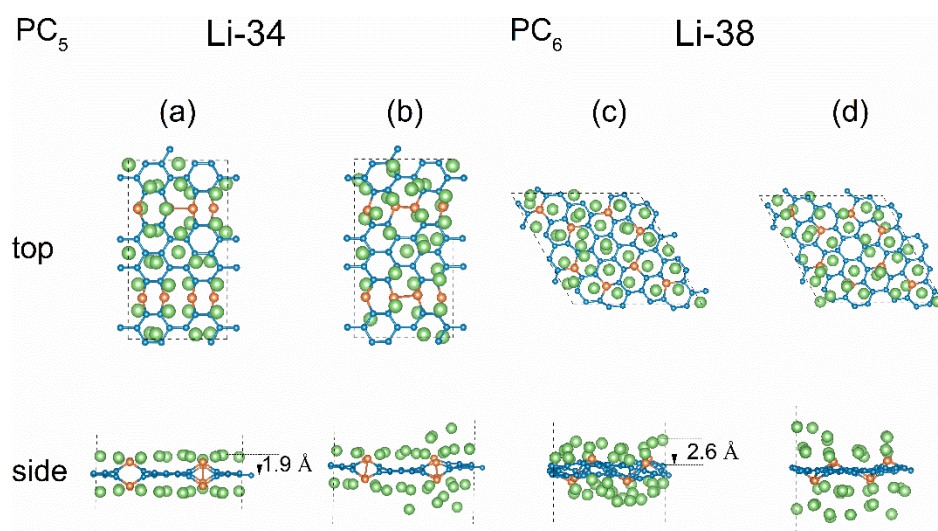


Fig. 6 Optimized structures before and after AIMD simulations (2 ps, 300 K) of Li-intercalated PC₅ and PC₆ (2×2 supercell) with maximum numbers of adsorbed Li atoms without deformation, including top and side view of P₈C₄₀Li₃₄ (a) before and (b) after AIMD simulation, and top and side view of P₈C₄₈Li₃₈ (c) before and (d) after AIMD simulation. The Li, P, and C atoms are distinguished by green, orange, and blue color, respectively.

4. Conclusion

In summary, we explore the potential applications of 2D PC_x ($x=2, 5, 6$) monolayers as the anode materials for Li-ion batteries by means of DFT calculations and *ab initio* molecular dynamics simulations. The most energetically favorable diffusion pathways for Li atom in PC_2 , PC_5 and PC_6 are identified with considerably low diffusion barriers of 0.18 eV, 0.47 eV and 0.44 eV, respectively, which in turn allows fast charge–discharge rates when they are used as anodes. In addition, PC_5 and PC_6 monolayer also exhibit high theoretical capacity values of 1251.7 mAh g⁻¹ and 1235.9 mAh g⁻¹, respectively, which are nearly three times that of graphite. These excellent properties suggest that the dynamically stable PC_5 and PC_6 monolayers could be promising anode materials. Our results give insightful prospects for further experimental work to explore carbon rich PC_x monolayers as promising electrode material for Li ion batteries.

AUTHOR INFORMATION

Notes

The authors declare no competing financial interests.

ACKNOWLEDGMENT

This work was supported by the Research Grants Council of the Hong Kong Special Administrative Region, China (Project No. PolyU152208/18E), the Hong Kong

Polytechnic University (Project Nos. RHA3), and Department of Science and Technology of Guangdong Province (Project No. 2019A050510012). X. L. thanks support from NSFC (No. 11804286) and the fundamental Research Funds for the central Universities.

REFERENCES

1. H. Chen, T. N. Cong, W. Yang, C. Tan, Y. Li and Y. Ding, *Prog. Nat. Sci.*, 2009, **19**, 291-312.
2. G. Ren, G. Ma and N. Cong, *Renewable Sustainable Energy Reviews*, 2015, **41**, 225-236.
3. L. Lu, X. Han, J. Li, J. Hua and M. Ouyang, *J. Power Sources*, 2013, **226**, 272-288.
4. G. Pistoia, *Lithium-ion batteries*, Newnes, advances and applications, 2013.
5. Z. Li, J. Huang, B. Y. Liaw, V. Metzler and J. Zhang, *J. Power Sources*, 2014, **254**, 168-182.
6. N. Nitta, F. Wu, J. T. Lee and G. Yushin, *Materials today*, 2015, **18**, 252-264.
7. Y. Zhong, M. Yang, X. Zhou and Z. Zhou, *Materials Horizons*, 2015, **2**, 553-566.
8. A. Kuzmenko, E. Van Heumen, F. Carbone and D. Van Der Marel, *Phys. Rev. Lett.*, 2008, **100**, 117401.
9. A. Luican, G. Li and E. Y. Andrei, *Solid State Commun.*, 2009, **149**, 1151-1156.
10. A. K. Geim and K. S. Novoselov, in *Nanoscience and Technology: A Collection of Reviews from Nature Journals*, World Scientific, 2010, pp. 11-19.
11. H. Li, R. Y. Tay, S. H. Tsang, W. Liu and E. H. T. Teo, *Electrochim. Acta*, 2015, **166**, 197-205.
12. M. T. F. Rodrigues, K. Kalaga, H. Gullapalli, G. Babu, A. L. M. Reddy and P. M. Ajayan, *Advanced Energy Materials*, 2016, **6**, 1600218.
13. S. Zhao, W. Kang and J. Xue, *J. Mater. Chem. A*, 2014, **2**, 19046-19052.
14. W. Li, Y. Yang, G. Zhang and Y.-W. Zhang, *Nano Lett.*, 2015, **15**, 1691-1697.
15. G.-C. Guo, D. Wang, X.-L. Wei, Q. Zhang, H. Liu, W.-M. Lau and L.-M. Liu, *J. Phys. Chem. Lett.*, 2015, **6**, 5002-5008.
16. M. Dixit, B. Markovsky, F. Schipper, D. Aurbach and D. T. Major, *J. Phys. Chem. C*, 2017, **121**, 22628-22636.
17. D. Er, J. Li, M. Naguib, Y. Gogotsi and V. B. Shenoy, *ACS Appl. Mater. Interfaces*, 2014, **6**, 11173-11179.
18. J. Hu, B. Xu, C. Ouyang, S. A. Yang and Y. Yao, *J. Phys. Chem. C*, 2014, **118**, 24274-24281.
19. K. Fan, Y. Ying, X. Li, X. Luo and H. Huang, *J. Phys. Chem. C*, 2019, **123**, 18207-18214.
20. V. Zinth, C. von Lüders, M. Hofmann, J. Hattendorff, I. Buchberger, S. Erhard, J. Rebelo-Kornmeier, A. Jossen and R. Gilles, *J. Power Sources*, 2014, **271**, 152-159.
21. B. Sa, Y.-L. Li, J. Qi, R. Ahuja and Z. Sun, *J. Phys. Chem. C*, 2014, **118**, 26560-26568.
22. J. Dai and X. C. Zeng, *J. Phys. Chem. Lett.*, 2014, **5**, 1289-1293.
23. G. Seifert and E. Hernandez, *Chem. Phys. Lett.*, 2000, **318**, 355-360.

24. B. Zhang and D. S. Su, *Small*, 2014, **10**, 222-229.
25. G. Wang, R. Pandey and S. P. Karna, *Nanoscale*, 2016, **8**, 8819-8825.
26. W. C. Tan, Y. Cai, R. J. Ng, L. Huang, X. Feng, G. Zhang, Y.-W. Zhang, C. A. Nijhuis, X. Liu and K.-W. Ang, *Adv. Mater.*, 2017, **29**, 1700503.
27. W. C. Tan, L. Huang, R. J. Ng, L. Wang, D. M. N. Hasan, T. J. Duffin, K. S. Kumar, C. A. Nijhuis, C. Lee and K. W. Ang, *Adv. Mater.*, 2018, **30**, 1700503.
28. W. Zhang, J. Yin, P. Zhang, X. Tang and Y. Ding, *J. Mater. Chem. A*, 2018, **6**, 12029-12037.
29. D. Singh, S. Kansara, S. K. Gupta and Y. Sonvane, *J. Mater. Sci.*, 2018, **53**, 8314-8327.
30. T. Yu, Z. Zhao, Y. Sun, A. Bergara, J. Lin, S. Zhang, H. Xu, L. Zhang, G. Yang and Y. Liu, *J. Am. Chem. Soc.*, 2019, **141**, 1599-1605.
31. K. Dou, Y. Ma, T. Zhang, B. Huang and Y. Dai, *Phys. Chem. Chem. Phys.*, 2019.
32. G. Kresse and J. Furthmüller, *Phys. Rev. B*, 1996, **54**, 11169.
33. J. P. Perdew, K. Burke and M. Ernzerhof, *Phys. Rev. Lett.*, 1996, **77**, 3865.
34. S. Grimme, *J. Comput. Chem.*, 2006, **27**, 1787-1799.
35. A. V. Krukau, O. A. Vydrov, A. F. Izmaylov and G. E. Scuseria, *The Journal of chemical physics*, 2006, **125**, 224106.
36. W. Tang, E. Sanville and G. Henkelman, *J. Phys.: Condens. Matter*, 2009, **21**, 084204.
37. G. Henkelman, B. P. Uberuaga and H. Jónsson, *J. Chem. Phys.*, 2000, **113**, 9901-9904.
38. A. Togo and I. Tanaka, *Scr. Mater.*, 2015, **108**, 1-5.
39. S. Nosé, *J. Chem. Phys.*, 1984, **81**, 511-519.
40. F. T. Hesselink, *J. Colloid Interf. Sci.*, 1977, **60**, 448-466.
41. E. Yang, H. Ji and Y. Jung, *J. Phys. Chem. C*, 2015, **119**, 26374-26380.
42. X. Zhang, Z. Yu, S.-S. Wang, S. Guan, H. Y. Yang, Y. Yao and S. A. Yang, *J. Mater. Chem. A*, 2016, **4**, 15224-15231.
43. X. Li, Q. Wang and P. Jena, *J. Phys. Chem. Lett.*, 2017, **8**, 3234-3241.
44. X. Zhang, J. Hu, Y. Cheng, H. Y. Yang, Y. Yao and S. A. Yang, *Nanoscale*, 2016, **8**, 15340-15347.
45. Y. Xie, Y. Dall'Agnese, M. Naguib, Y. Gogotsi, M. W. Barsoum, H. L. Zhuang and P. R. C. Kent, *J. Am. Chem. Soc.*, 2014, **8**, 9606-9615.
46. S. Wang, B. Yang, H. Chen and E. Ruckenstein, *J. Mater. Chem. A*, 2018, **6**, 6815-6821.
47. A. Savin, R. Nesper, S. Wengert and T. F. Fässler, *Angewandte Chemie International Edition in English*, 1997, **36**, 1808-1832.
48. S. Noury, X. Krokidis, F. Fuster and B. Silvi, *Computers chemistry*, 1999, **23**, 597-604.
49. J. K. Burdett and T. A. McCormick, *J. Phys. Chem. A*, 1998, **102**, 6366-6372.
50. V. Tsirelson and A. Stash, *Chem. Phys. Lett.*, 2002, **351**, 142-148.
51. E. Lee and K. A. Persson, *Nano Lett.*, 2012, **12**, 4624-4628.
52. Q. Meng, A. Hu, C. Zhi and J. Fan, *Phys. Chem. Chem. Phys.*, 2017, **19**, 29106-29113.
53. T. Yu, Z. Zhao, L. Liu, S. Zhang, H. Xu and G. Yang, *J. Am. Chem. Soc.*, 2018, **140**, 5962-5968.
54. C.-S. Liu, X.-L. Yang, J. Liu and X.-J. Ye, *ACS Appl. Energy Mater.*, 2018, **1**, 3850-3859.
55. Q. Meng, J. Ma, Y. Zhang, Z. Li, C. Zhi, A. Hu and J. Fan, *Nanoscale*, 2018, **10**, 3385-3392.

Supporting Information

Theoretical investigation of two-dimensional phosphorus carbides as promising anode materials for lithium-ion batteries

*Ke Fan^a, Yiran Ying^a, Xin Luo^b, and Haitao Huang^{*a}*

^aDepartment of Applied Physics, The Hong Kong Polytechnic University, Hung Hom, Kowloon,
Hong Kong, P.R. China

^bSchool of Physics, Sun Yat-sen University, Guangzhou, Guangdong Province, P.R. China,
510275

AUTHOR INFORMATION

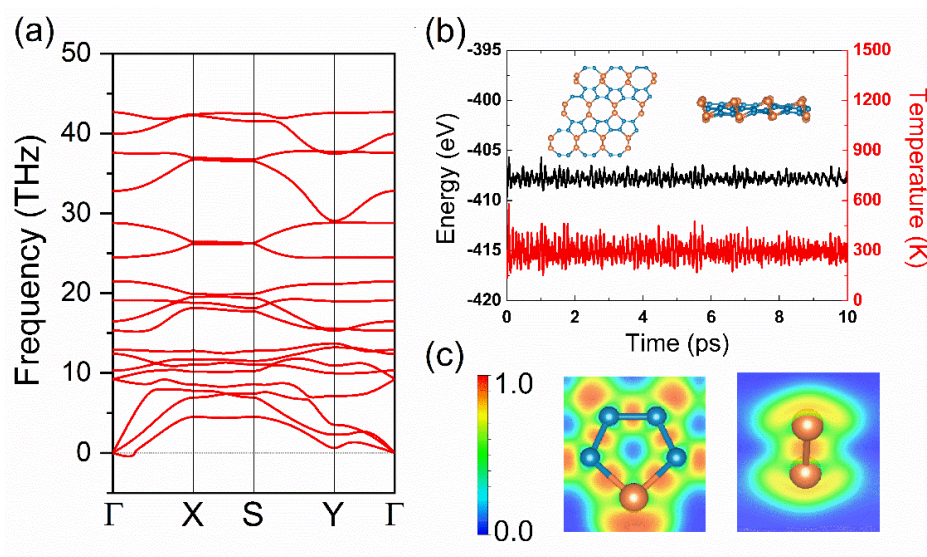
Corresponding Author

*E-mail: aphhuang@polyu.edu.hk (H.H.); luox77@mail.sysu.edu.cn (X.L.)

Table S1. Structural information (lattice constants, bond length, and bond angle) of PC_x systems

	PC_2	PC_5	PC_6
$a(\text{\AA})$	3.96	4.39	6.69
$b(\text{\AA})$	5.27	7.86	6.69
Rc-c(\AA)	1.40, 1.43	1.39, 1.43, 1.46	1.37, 1.42, 1.46
Rc-p(\AA)	1.82	1.82	1.81
Rp-p(\AA)	2.27	2.12	
α	86.89	88.87	90.00
β	91.70	94.31	90.00
γ	67.95	89.99	120.00

PC₂



PC₆

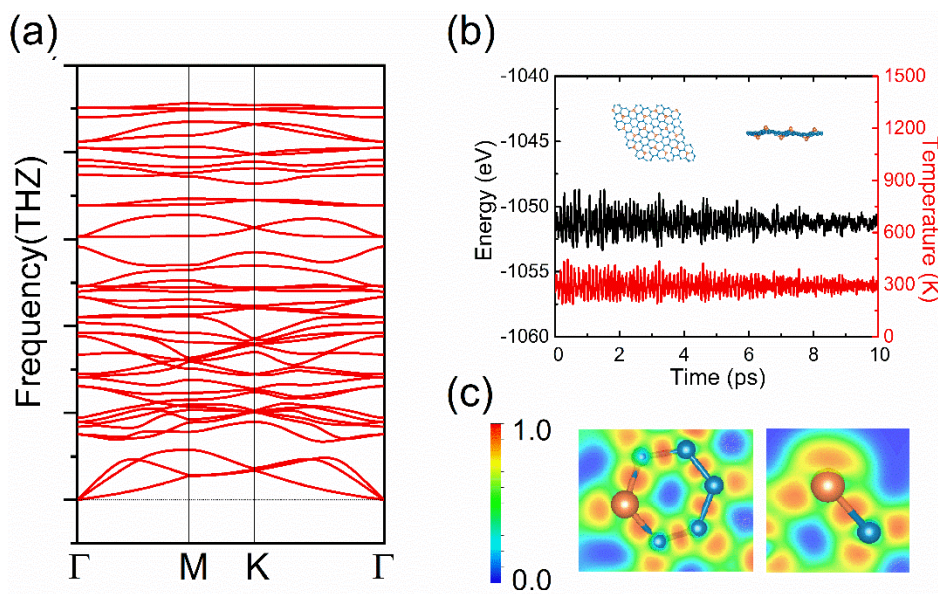


Fig. S1 Phonon dispersion spectra, AIMD simulation and ELF maps of PC₂ and PC₆.

The P atoms and C atoms are distinguished by orange and blue color, respectively.

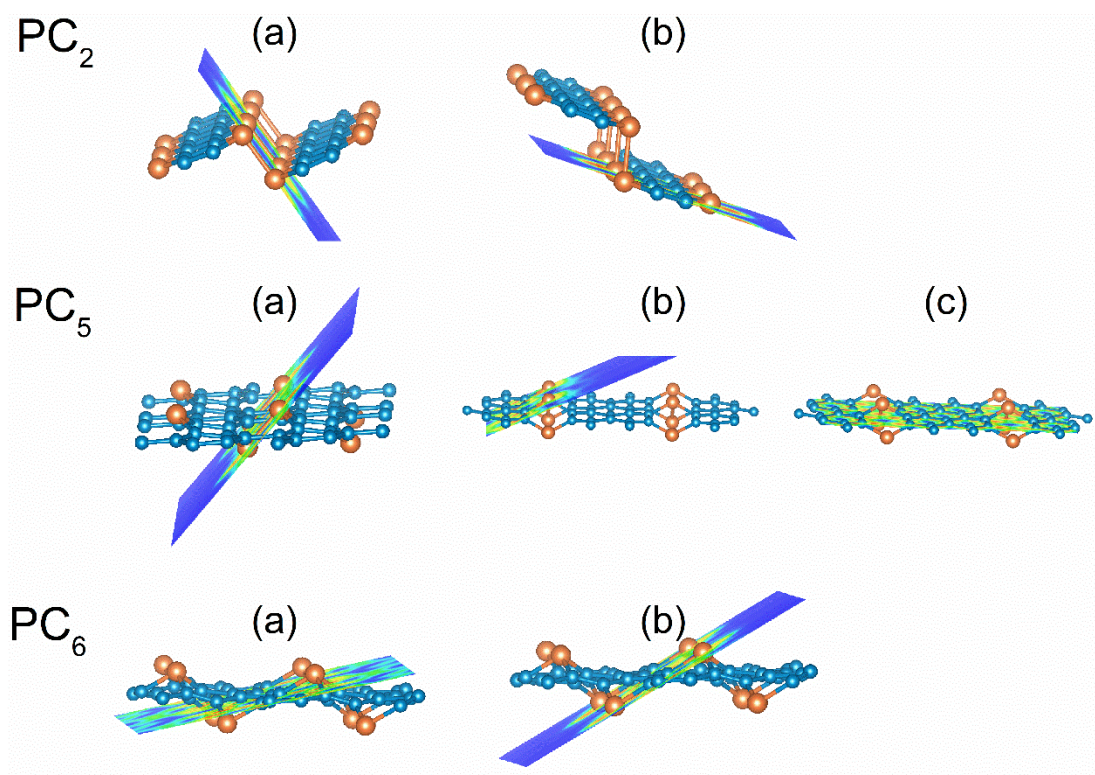
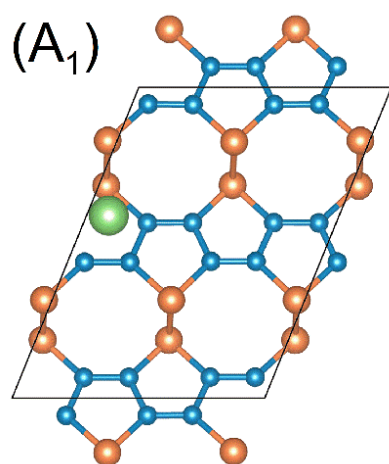
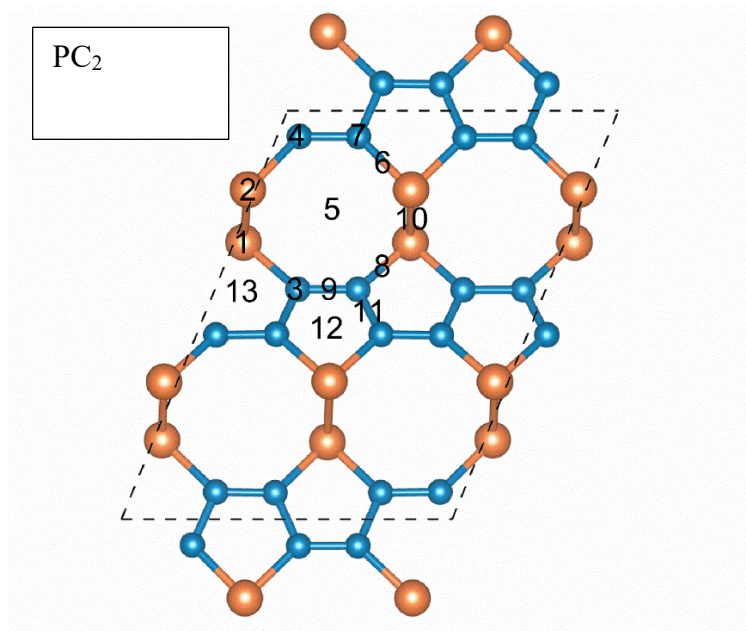
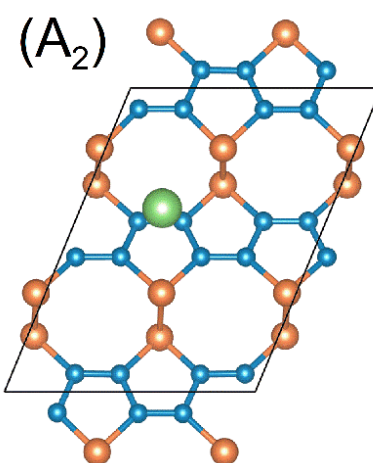


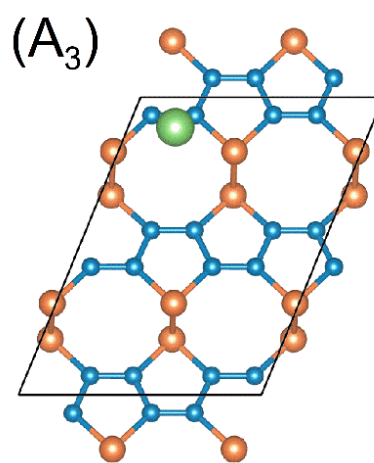
Fig. S2 Schematic illustration of the crystallographic orientation direction along planes containing specified bonding atoms of PC_x system. The P atoms and C atoms are distinguished by orange and blue color, respectively.



$$\Delta E_1 = -0.93 \text{ eV}$$

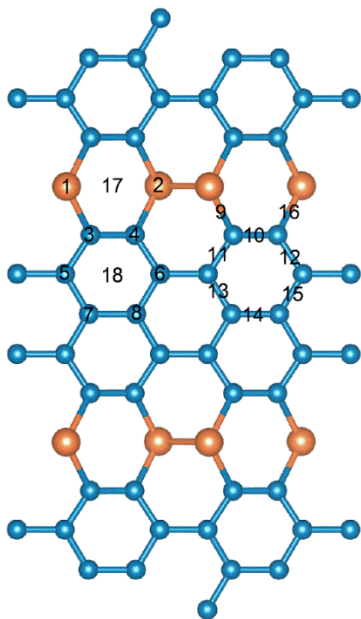


$$\Delta E_2 = -0.87 \text{ eV}$$

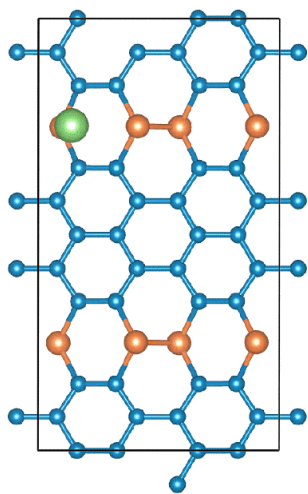


$$\Delta E_3 = -0.43 \text{ eV}$$

PC₅

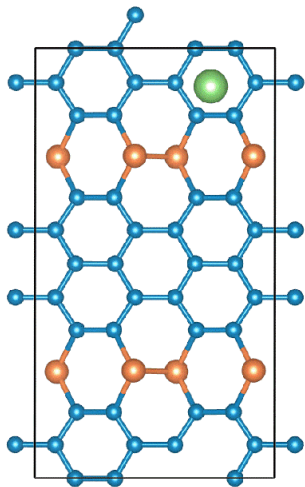


(A₁)



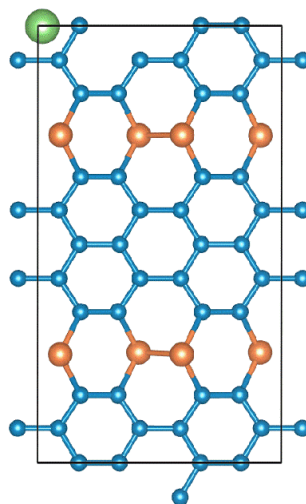
$$\Delta E_1 = -0.83eV$$

(A₂)



$$\Delta E_2 = -0.67eV$$

(A₃)



$$\Delta E_3 = -0.57eV$$

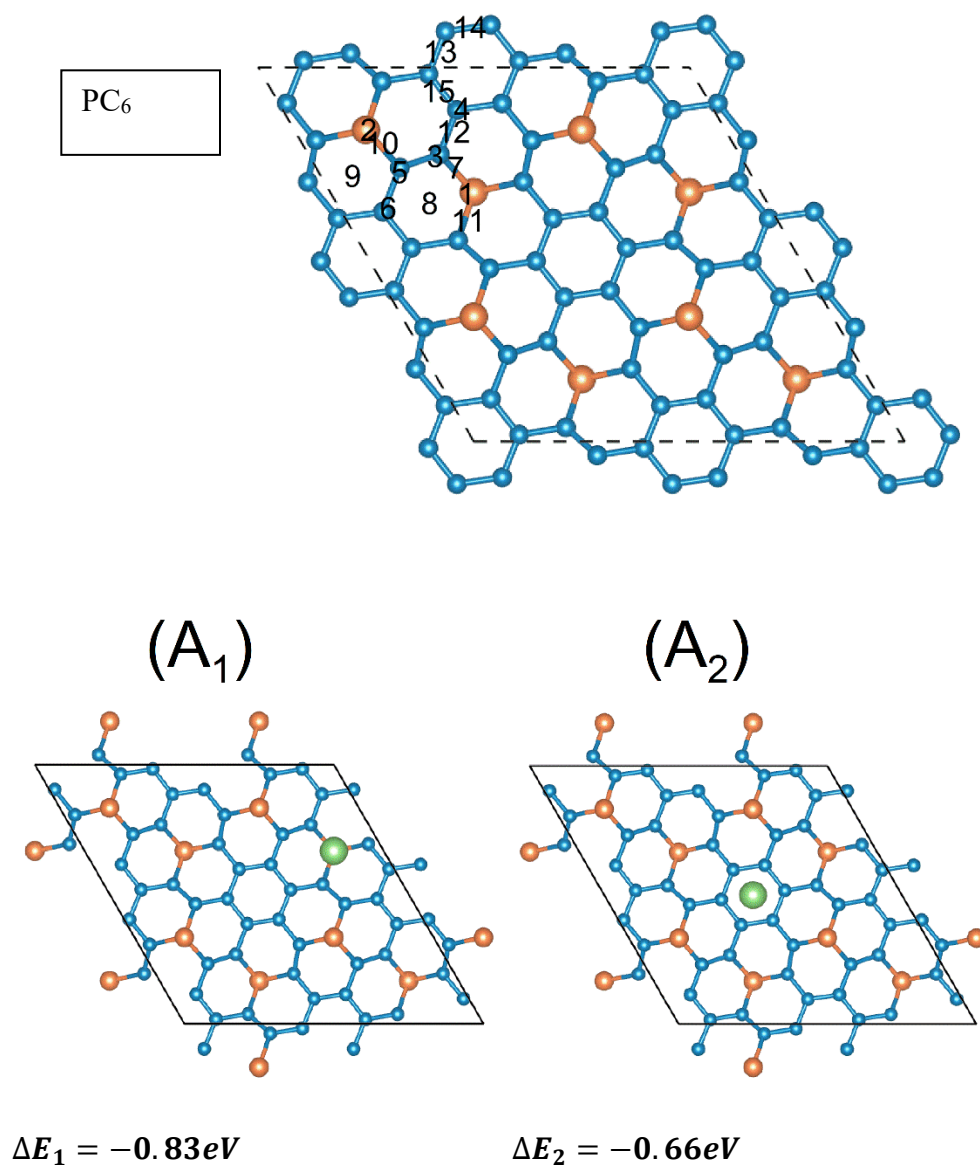


Fig. S3 Geometric structure of possible adsorption sites on PC₂, PC₅, and PC₆ monolayer. The adsorption energy values for Li atom adsorbed on each site are listed below the corresponding figures. The Li, P, and C atoms are distinguished by green, orange, and blue color, respectively.

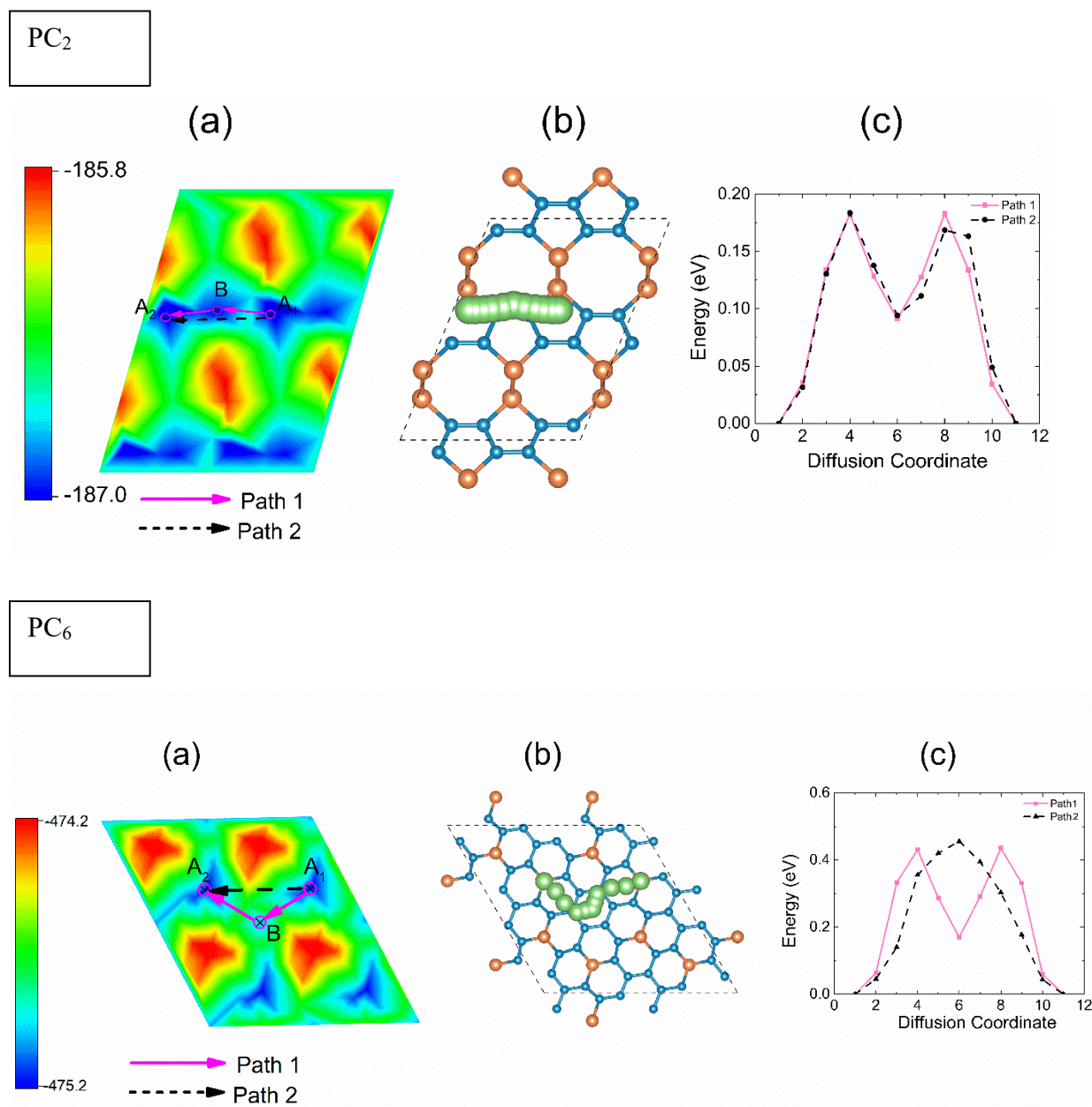


Fig. S4 (a) Schematic illustration of three possible paths for Li diffusion on the PC₂ and PC₆ monolayer based on the color-filled contour plots of adsorption energy of single Li atom on the surface; (b) Diffusion of single adatoms over PC₂ and PC₆ monolayer through the favorable pathways (path 1). (c) The corresponding diffusion barrier profiles of Li-PC₅ and Li-PC₆ monolayer. The Li, P, and C atoms are distinguished by green, orange, and blue color, respectively.

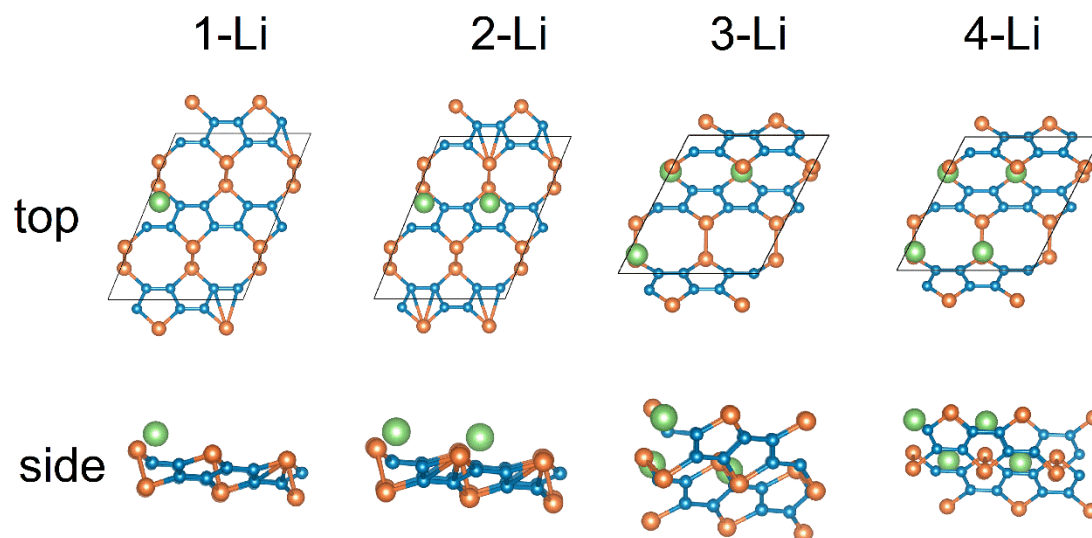


Fig. S5 Optimized structure of different numbers of Li-intercalated PC_2 monolayers ($\text{P}_8\text{C}_{16}\text{Li}$, $\text{P}_8\text{C}_{16}\text{Li}_2$, $\text{P}_8\text{C}_{16}\text{Li}_3$ and $\text{P}_8\text{C}_{16}\text{Li}_4$) from top and side view. The Li, P, and C atoms are distinguished by green, orange, and blue color, respectively.

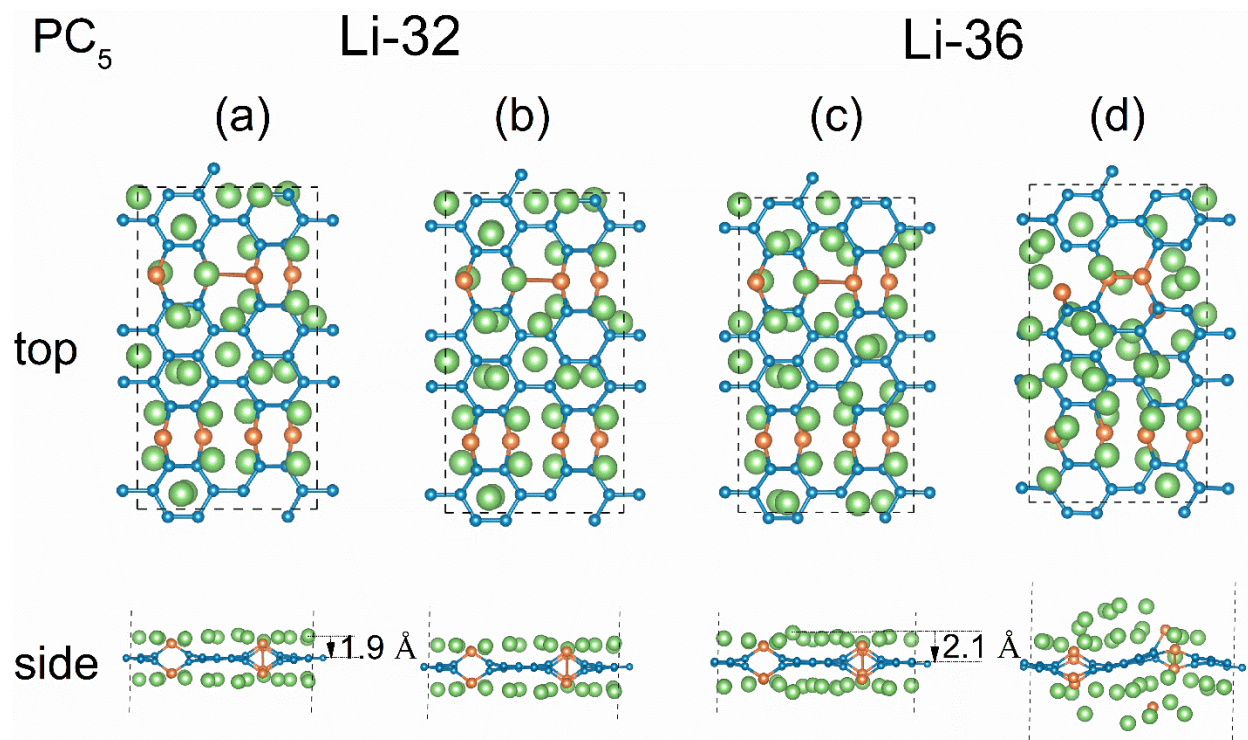


Fig. S6 Optimized structures of different Li-intercalated PC₅ monolayer (2×2 supercell), including P₈C₄₀Li₃₂ (a) before and (b) after AIMD simulations, and P₈C₄₀Li₃₆ (c) before and (d) after AIMD simulations (300 K). The Li, P, and C atoms are distinguished by green, orange, and blue color, respectively.

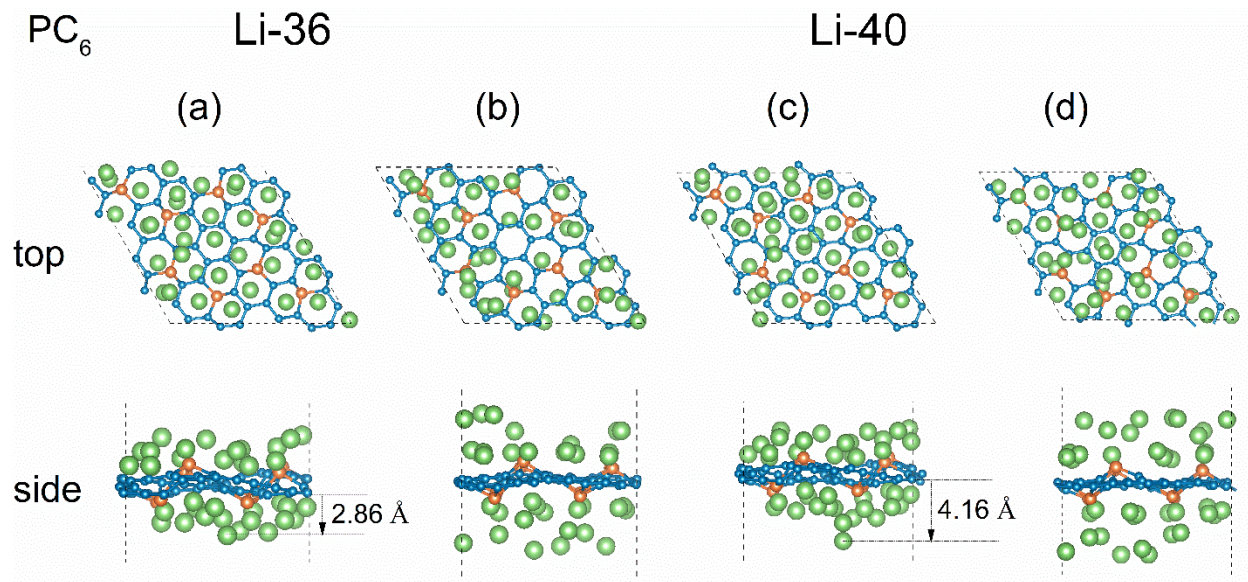


Fig. S7 Optimized structures of different Li-intercalated PC₆ monolayers (2×2 supercell), including P₈C₄₈Li₃₆ (a) before and (b) after AIMD simulations, and P₈C₄₈Li₄₀ (c) before and (d) after AIMD simulations (300 K). The Li atoms, P atoms and C atoms are distinguished by green, orange, and blue color, respectively.

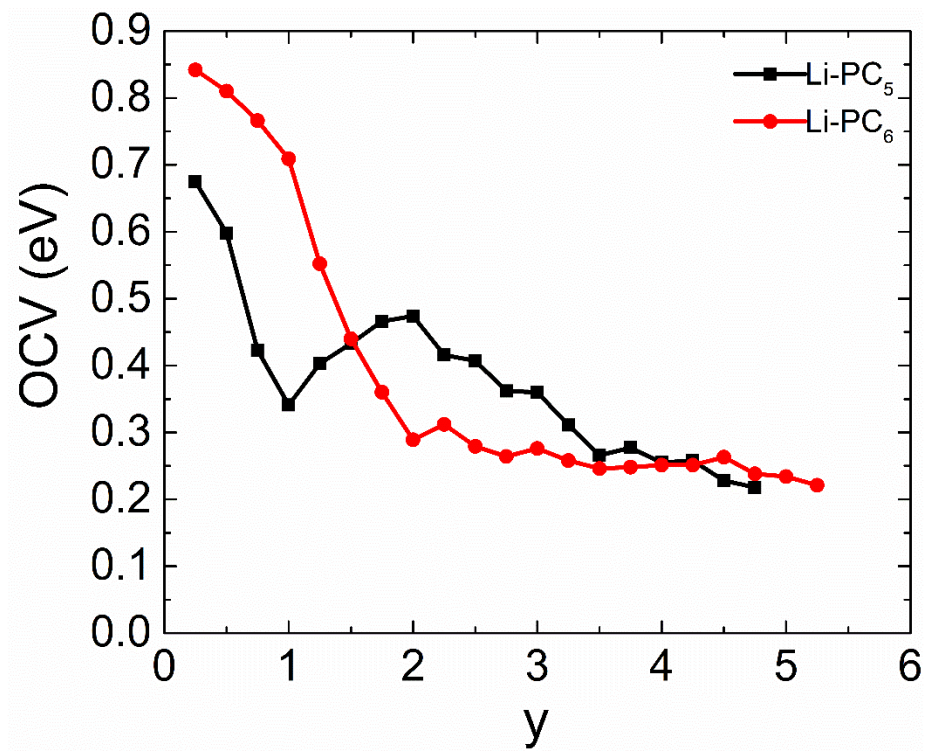


Fig. S8 Open-circuit voltage (OCV) as a function of adatom content y for PC_5 and PC_6 .